Experimental Mechanics
https://doi.org/10.1007/s11340-018-00465-0

Characterization of the Effects of Internal Pores on Tensile Properties of Additively Manufactured Austenitic Stainless Steel 316L

A.E. Wilson-Heid[1] · T.C. Novak[1] · A.M. Beese[1,2]

Received: 14 September 2018 / Accepted: 27 November 2018

Abstract
In this study, the effects of internal pores on the tensile behavior of austenitic stainless steel 316L manufactured with laser powder bed fusion (L-PBF) additive manufacturing (AM) were investigated. Both fully-dense samples and samples with intentional internal pores of varying diameters were fabricated. For each sample with a pore, the internal pore was deliberately fabricated in the center of the cylindrical tensile sample during AM processing. By varying the diameter of the 180 μm-tall initial penny-shaped pores, from 150 to 4800 μm within 6 mm gauge diameter cylindrical samples, the impact of lack-of-fusion, commonly present in AM, as well as the impact of well-defined pores in general, on tensile mechanical properties was studied. To link the pore size and morphology to the mechanical properties, the sizes of the initial pores were evaluated using non-destructive Archimedes measurements, 2D X-ray radiography, 3D X-ray computed tomography, and destructive 2D optical microscopy. Samples with and without the single, penny-shaped pore were subjected to uniaxial tension to evaluate the defect size dependent mechanical properties. The intentional pore began to impact ultimate tensile strength when the pore diameter was 2400 μm, or 16% of the cross-sectional sample area. Elongation to failure was significantly affected when the pore diameter was 1800 μm or 9% of the cross-sectional sample area. This shows that 316L stainless steel manufactured by additive manufacturing is defect-tolerant under uniaxial tension loading.

Keywords Additive manufacturing · 316L stainless steel · Porosity · X-ray computed tomography · Tensile properties · Ductility

Introduction

Additive manufacturing (AM) is a layer-by-layer manufacturing process used to create three-dimensional (3D) components [1]. In laser powder bed fusion (L-PBF) AM, a laser power source is used to rapidly melt and fuse metal powder feedstock one layer at a time to form a 3D component. Once a layer has been completed, the build plate is lowered, a new layer of powder is spread over the previous layer(s), and the lasing/powder addition process is repeated until the component is finished [2, 3]. In AM, internal defects and heterogeneous microstructures, caused by rapid solidification and thermal cycling, are frequently present [1]. Understanding how the microstructure and defects affect the mechanical behavior of components is required in order to design against failure in components made by AM. This includes understanding which techniques are best for characterizing defects and determining tolerable limits of defects within AM components that still result in structurally sound parts.

Components fabricated by AM may contain internal porosity either from processing defects or raw material defects [4]. More specifically these pores are usually caused by gas entrapment, keyholing, or lack-of-fusion (LoF) between subsequent laser passes or layers in the L-PBF process [2, 5–7]. Gas entrapment defects, which are commonly spherical in morphology and can range from 10 to 130 μm in diameter [8, 9], have been proposed to persist from the pores present in the original powder feedstock for particles that do not completely remelt [10], from the collapse of keyhole vapor cavities caused by excessive energy input [7], or with an analogous mechanism as casting pores where there is evolution of dissolved gases from the liquid during solidification [11]. The presence of small gas pores caused by excessive energy input have been found to not impact the strength and ductility of material when present in amounts up to 1 vol.% for Ti-6Al-4 V built via L-PBF [12].

Allison Beese is a member of the Society for Experimental Mechanics.

✉ A. M. Beese
amb961@psu.edu

[1] Department of Materials Science and Engineering, Pennsylvania State University, University Park, PA 16802, USA

[2] Department of Mechanical Engineering, Pennsylvania State University, University Park, PA 16802, USA

Published online: 14 December 2018

However, LoF pores, which can range from 15 to 600 μm [9, 13, 14] and are irregular in morphology, have been shown to be detrimental to mechanical properties of materials because their sharp features act as stress concentration sites [12, 14, 15]. Carlton et al. evaluated the role of LoF pores on tensile behavior of L-PBF stainless steel 316L using in situ X-ray computed tomography (CT) testing and found that samples with high porosity (>2.2%) displayed flaw-driven failure where cracks initiated at pre-existing defects [14]. Stef et al. found that the formation of these pores are closely related to the laser scan pattern, where LoF porosity is more common in areas where the overlapping of the laser scan pattern exists between sequential layers [16]. Spierings et al. showed that increased scanning speed from 300 to 850 mm/s at a constant power of 104 W resulted in an increase of LoF porosity formation and overall porosity of 0.03% to 9.02% for stainless steel 316L samples built with L-PBF [17], highlighting the importance of using optimized process parameters. Although it is known that LoF pores negatively impact the mechanical behavior of AM components, quantifying the impact of internal pores on tensile ductility is important for defining defect tolerances in AM.

The role of internal pores on the mechanical properties of ductile metals is of interest to not only the AM community, but to the entire fracture community. There has been much classical research on the role of pores in ductile plasticity [18, 19] and fracture, including theoretical work on the growth of spherical voids [20] and cylindrical voids [21]. In AM the layer-by-layer processing can be used to intentionally manufacture internal pores into samples, which is not possible with conventional manufacturing techniques, in order to directly assess the impact of void size on ductile fracture. Fadida et al. [22] embedded a single spherical pore at the center of 4 mm diameter Ti-6Al-4V dynamic tensile samples manufactured via L-PBF and found that samples with a 600 μm or greater diameter pore had significantly lower tensile ductility compared to dense samples. They also showed that at this critical pore diameter (with respect to sample gauge diameter), the failure in samples always occurred at the pore location. Conversely, the failure location did not necessarily correspond to the pore location for pores smaller than 600 μm in diameter. Li et al. studied the effect of random porosity (i.e., not a single well-defined pore) in tensile specimens by changing the laser scanning speed and maintaining constant laser power of 100 W in the manufacturing of 316L by L-PBF samples [5]. A scanning speed of 90 mm/s correlated to a density of greater than 95% and an ultimate tensile strength (UTS) of 650 MPa, while the sample with a scanning speed of 180 mm/s had a density of 65% and UTS below 50 MPa. With AM, the effect of pores can be isolated to determine their impact on mechanical properties giving insight to void growth in both AM and conventional materials.

The presence of internal defects can be assessed and quantified using different methods. The classic Archimedes method has been used to quantify bulk porosity in AM components [23, 24]. This method is non-destructive, but the results can vary based on part surface finish and surface-breaking porosity [17]. The Archimedes method provides bulk porosity information, but does not provide information about pore size distribution, pore locations, or pore morphology, all which have been found to be important factors when assessing mechanical properties [14]. X-ray radiography (2D) and X-ray CT (3D) are also non-destructive methods for investigating internal porosity. In 2D radiography, a shadowgraph of a stationary 3D sample is produced by directing radiation energy through a sample and measuring attenuation with a detector on the opposite side. This method can be used to assess variations in 2D grayscale projections of the sample that can be generated quickly to provide for assessment of pore cross-sections.

In X-ray CT, the sample is rotated in angular increments ranging from 0° to 360° and is exposed to the source generated X-rays. The attenuated X-rays are captured by a detector and a mathematical algorithm is used to convert the 2D data into a 3D reconstruction of the entire sample or region of interest [25]. In X-ray CT the size of quantifiable pores in a sample is directly related to the voxel size that is used in the analysis, where pores smaller than the voxel size cannot be measured [25], and typically, the convention is to assume that any pores that can be reliably detected are three times the voxel size or larger. Voxel size is dictated by the desired magnification or field of view [26]. This is an important consideration when determining the desired scan resolution and a compromise must be made between desired porosity resolution, volume of area analyzed, time, and economics [26]. The biggest benefit of using X-ray CT is that it can be used to non-destructively characterize the 3D morphology of pores, the spatial distribution (and location) of pores, and the distribution of pore sizes in a metallic sample.

For destructive evaluation of pores, serial sectioning with optical microscopy may be used. With this method only one 2D cross-section of a component can be analyzed at a time, providing limited information on pore size, morphology, and distribution. This method is prone to selection bias and the appropriate magnification must be selected to achieve consistent pore resolution [17].

The aim of the present study was to isolate the role of internal pores on the tensile properties of austenitic stainless steel samples made using L-PBF and provide a direct understanding of the impact of initial void size on the tensile properties of conventional materials. A secondary aim was to compare different methods used to quantify porosity in manufactured components. Leveraging the unique capabilities of AM, samples were manufactured with a penny-shaped internal pore, at the center of cylindrical tensile specimens, to mimic the presence of a LoF pore or large pores formed during

void growth. Four different methods were used to measure the embedded pore size and morphology. By changing the size of the pores within samples, the role of defect size on tensile mechanical properties was investigated.

Experimental

Fabrication

In this study, a ProX DMP 320 laser powder bed fusion machine by 3D Systems [27] was used to manufacture AISI Type 316L Stainless Steel (316L) round cylindrical samples. The processing parameters used to fabricate the 316L L-PBF cylinders are shown in Table 1. The powder was sieved using a 60 μm screen. The composition of the fabricated 316L material, shown in Table 2, was measured using combustion infrared detection for carbon and sulfur content (ASTM E1019–18, [28]), inert gas fusion for nitrogen content (ASTM E1019–18, [28]), and direct current plasma emission spectroscopy for all other elements (ASTM E 1097–12, [29]). Cylindrical samples with an external diameter of 10 mm were built in the vertical orientation, such that when machined to tensile specimen geometry the loading axis was parallel to the vertical build direction. Each cylinder, except for the fully dense samples, had a single, centrally located pore, designed to be 180 μm tall, to closely mimic the sharp features in LoF pores. Specimens with eleven different pore diameters, whose dimensions are in Table 3, and fully dense specimens were fabricated. The cylinders were removed from the baseplate using wire electrical discharge machining in the as-built condition, as stress-relief has been shown to have no significant effect on mechanical properties of L-PBF 316L [30]. Samples were then machined to the cylindrical tensile geometry in Fig. 1 using a CNC lathe to remove the effect of surface finish, which has been shown to impact the mechanical behavior of AM components [32].

In addition to the cylindrical tensile test samples, a cylindrical witness sample that contained all eleven penny-shaped pore geometries was fabricated as shown in Fig. 2. This sample was used to characterize pore size and morphology using X-ray CT and cross-section analysis after machining to a 6 mm diameter, which is equivalent to the tensile sample gauge diameter. The characterized geometries in the witness samples were assumed to be representative of those in the corresponding tensile test samples.

Table 1 Processing parameters used for L-PBF manufacturing of 316L samples in the present study

Laser Power (W)	Layer thickness (μm)	Hatch spacing (μm)	Scanning speed (mm/s)
300	60	100	900

Table 2 Chemical composition (wt.%) of the as-built stainless steel 316L in the present study

Element	
Carbon, C	0.02
Manganese, Mn	0.79
Phosphorous, P	0.008
Sulfur, S	0.006
Silicon, Si	0.60
Chromium, Cr	17.80
Nickel, Ni	12.48
Molybdenum, Mo	2.41
Nitrogen, N	0.068
Iron, Fe	Bal.

Archimedes Method

The Archimedes method was used to determine sample density and porosity of all machined tensile samples. The Archimedes process involved weighing the samples in the dry state to obtain their dry mass, m_{dry}, on an analytical balance (Ohaus Adventurer, Model AX324) that had a precision of 0.1 mg. Samples were then submerged in reverse osmosis (RO) water (ρ_{theor} assumed to be 1.0 g/cm^3) and put under vacuum for 24 h, during which the air bubbles on the surface of the samples were removed after 12 h to allow the water to continue to permeate the surface. After removal from the vacuum, samples were weighed while submerged in RO water to obtain m_{sub}, and then weighed in air after patting the samples dry to remove water on the surface, obtaining m_{soak}. All mass measurements were done at room temperature, each sample was measured five times in each state, and the scale was given time to reset to zero between measurements. Experimental density was calculated using the following equation:

$$\rho = \frac{m_{dry} \times \rho_{theor}}{m_{soak} - m_{sub}} \quad (1)$$

A theoretical density for 316L of 7.99 g/cm^3 was assumed for all calculations of experimentally determined porosity [33].

2D Radiograph Method

The cylindrical witness sample (Fig. 2), which contained all pore geometries studied, was analyzed with a General Electric v|tome|x L300 nano/microCT system. Two 2D radiograph images were taken for each pore in two perpendicular directions with the parameters in Table 4. The X-ray source was adjusted to be normal to each of the eleven pores when the grayscale image was taken to avoid skew in the data and in the measurement of the pore in post-process analysis, as shown in

Table 3 Diameters of 180 μm tall penny-shaped pores designed into the cylindrical tensile samples

Sample Name	Pore diameter (μm)	% of cross-sectional area of tensile sample	Pore diameter as measured by X-ray CT (μm)
B	150	0.06%	–
C	300	0.25%	282 ± 40
D	450	0.56%	455 ± 45
E	600	1%	538 ± 41
F	1200	4%	1135 ± 54
G	1800	9%	1781 ± 48
H	2400	16%	2373 ± 54
I	3000	25%	2961 ± 53
J	3600	36%	3595 ± 52
K	4200	49%	4132 ± 76
L	4800	64%	4789 ± 52

Fig. 3. ImageJ analysis software was used to measure the diameter and height of each pore in each 2D radiograph [34].

X-Ray CT Method

The same system and scan parameters that were used for 2D radiographs were used for the 3D X-ray computed tomography scan. A total of 1000 images, through rotations between 0° and 360°, were taken during the scan with an exposure time of 500 ms for each image and an averaging of three images per rotation. A voxel size of 13.45 μm was used, resulting in a minimum resolvable pore size of 40.35 μm [35]. The voxel size was calibrated prior to each scan using a calibration specimen with a known distance between the center of two ruby spheres; a correction was applied to the system after this calibration. These 2D images were reconstructed into a 3D dataset using the cone-beam algorithm developed by Feldkamp et al. [36]. The 32-bit reconstructed projections were imported to Avizo 9.3.0 software (Thermo Fisher Scientific) for 3D processing and analysis. The diameter for each intentionally introduced pore was measured from the

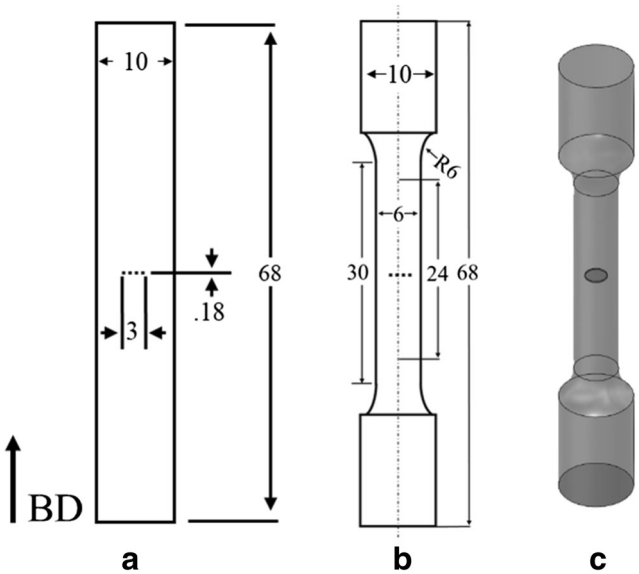

Fig. 1 Cross-section geometry of (**a**) as-built cylinders and (**b**) uniaxial tension samples in compliance with ASTM E8 [31], where dashed horizontal line indicates the intentionally introduced pore (here, showing a 3 mm diameter pore) at the center of the specimen. Dimensions in mm. (**c**) 3D CAD rendering of a tensile sample with an internal penny-shaped pore

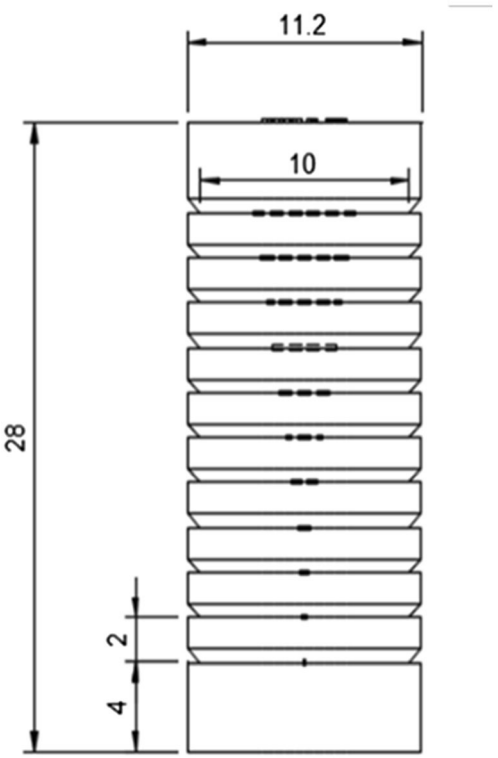

Fig. 2 Witness sample with pores vertically positioned every 2 mm, starting with the 150 μm closest to the baseplate and the 4800 μm farthest from the baseplate. The pore diameter/volume fractions in the witness sample were characterized with each porosity analysis technique. Dimensions in mm

Table 4 Parameters used in X-ray 2D radiographs and 3D computed tomography scans

Voxel size (μm)	Voltage (kV)	Current (mA)	Power (W)	Cu detector filter thickness (mm)	X-ray source to detector distance (mm)	Exposure time (ms)	Number of projections
13.45	150	90	13.5	0.5	500	500	1000

scan. As X-ray CT provides full information on pore morphology and size, the diameter of each pore measured with this technique was assumed to be the pore diameter in the corresponding tensile specimen, for the respective pore geometry, and the other pore measurement methods were compared against this measurement technique.

2D Cross-Section Method

After non-destructive evaluations of pore geometries, the witness sample was sectioned in half, parallel to the vertical build direction, to expose the pores for optical microscopy (OM) analysis. Half of the sample was mounted in epoxy, ground and polished using SiC abrasive papers, with a final polishing step using 0.05 μm colloidal silica. Images of the pores in the sample were taken using a digital optical microscope (Keyence VHX- 2000). ImageJ software was used to analyze the cross-section images by first converting the images to a 16-bit greyscale image, as shown in Fig. 4, and then a threshold value was used to distinguish between pores and solid material. The pore diameter and height were then measured using the modified image.

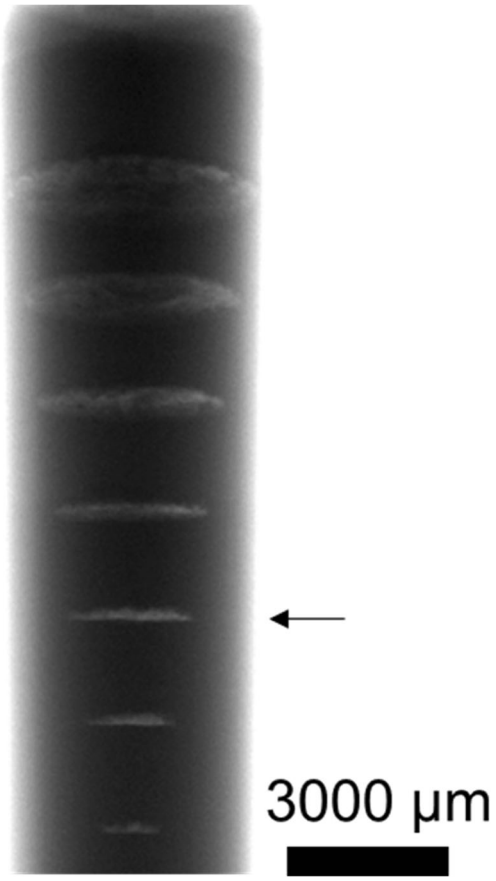

Fig. 3 2D radiograph image centered at the 1800 μm diameter pore, as indicated by the arrow. Each pore was centered with respect to the X-ray source for dimensional analysis to eliminate skewing, as seen in the larger pores in this image

Evaluation of Uncertainty

In the measurement of the internal pore diameters with the different techniques, the uncertainty in the measurements was quantified to account for the different origins of uncertainty in each of the techniques evaluated. For the measurement of the diameters of the pores using X-ray CT, the pores in the witness sample were reconstructed with Avizo software [37]. The volumetric center of each pore was calculated and its z-slice number (height in the vertical build direction) was determined. The diameter of the pore was measured with a best-fit a circle on the 2D cross-section where the volumetric center was calculated to be. The best-fit diameter was adjusted and measured at eight equally spaced distances around the pore using the best-fit circle. For each of the eight measurements an individual percent systematic error, $\delta_{i,sys}$, was calculated using:

$$\delta_{i,sys} = \frac{3 \times voxel\ size}{d_{mean}} \tag{2}$$

where d_{mean} is the mean diameter of the pore of interest as measured by the best-fit circle and the general rule for detectable features in a CT scan of three times the voxel size was used in the numerator [35]. The overall systematic error, $\delta_{o,sys}$, for a given pore was defined as:

$$\delta_{o,sys} = d_{mean} \times \frac{\sum \delta_{i,sys}}{n} \tag{3}$$

where n is the number of measurements. Random uncertainty, δ_{ran}, was defined as the standard deviation of the mean, using the standard deviation with Bessel's correction. Total uncertainty, δ_{tot}, which was used in the calculation of uncertainty in the percent difference as described later, was defined as:

$$\delta_{tot} = \sqrt{(\delta_{ran})^2 + (\delta_{o,sys})^2} \tag{4}$$

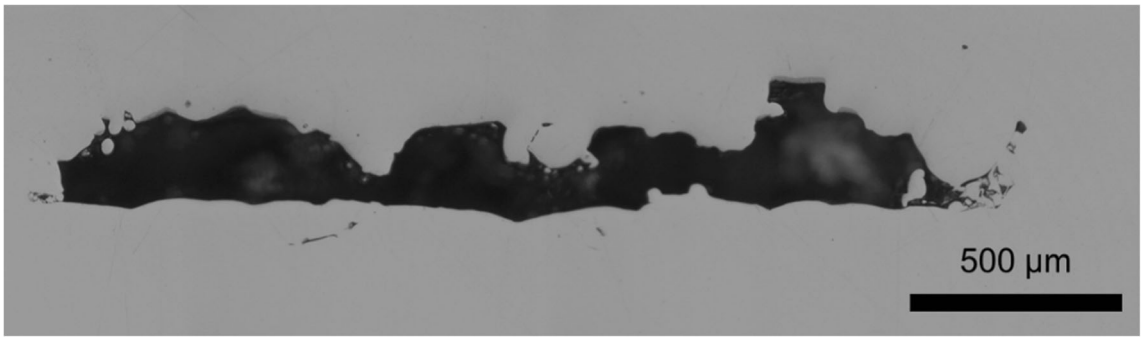

Fig. 4 Polished cross-section of the 2400 μm internal pore in the witness sample, which was used to measure dimensions for 2D cross-section analysis in ImageJ

For the 2D analysis techniques, measurements of the pore diameters were made in ImageJ software with the line tool and length was recorded in pixels. For the 2D radiograph images, three measurements of the pore diameter were made at different heights on the pore on the two perpendicular planes for a total of six measurements. Evaluating two perpendicular planes in 2D radiography analysis provides both more measurements and a more accurate assessment of the uncertainty in the measurements as shown in Fig. 5. For the 2D cross section method, five measurements of the pore diameter were made at different locations along the height of the pore. In both methods, at the edge of the pore there was a gradient of pixel colors, or grayscale, that could be considered the edge of the pore. The number of pixels in the gradient on one edge was recorded and multiplied by two to account for the uncertainty in the defined edge location at both sides of the measurement line. The ratio of total pixel gradient, d_{grad}, to the line length in pixels, d_l, was calculated for each line, and was defined as the individual systematic error $\delta_{i,sys}$:

$$\delta_{i,sys} = \frac{d_{grad}}{d_l} \tag{5}$$

In 2D cross-section analysis, this gradient was assumed to be the same for each of the five measurements of pore diameter. For the 2D radiography measurements, the gradient and therefore pixel ratio was redefined for each of the six measurements. The overall systematic error for a single pore was calculated using eq. (3). The random uncertainty for the 2D methods was calculated with the same methodology used for the X-ray CT. The total uncertainty was taken to be the systematic error and random uncertainty added in quadrature, as given in eq. (4).

The equation for percent difference, q, was used to compare the 2D measurements against the X-ray CT measurements, and is given as:

$$q = \frac{|x_{2D} - y_{XCT}|}{\left(\frac{x_{2D} + y_{XCT}}{2}\right)} \times 100 \tag{6}$$

where x_{2D} was the diameter of the pore as measured by the cross-section or 2D radiography method and y_{XCT} is the diameter of the pore as measured by X-ray CT method. The percent difference equation is an equation of two variables where each variable has an associated total uncertainty. To propagate the

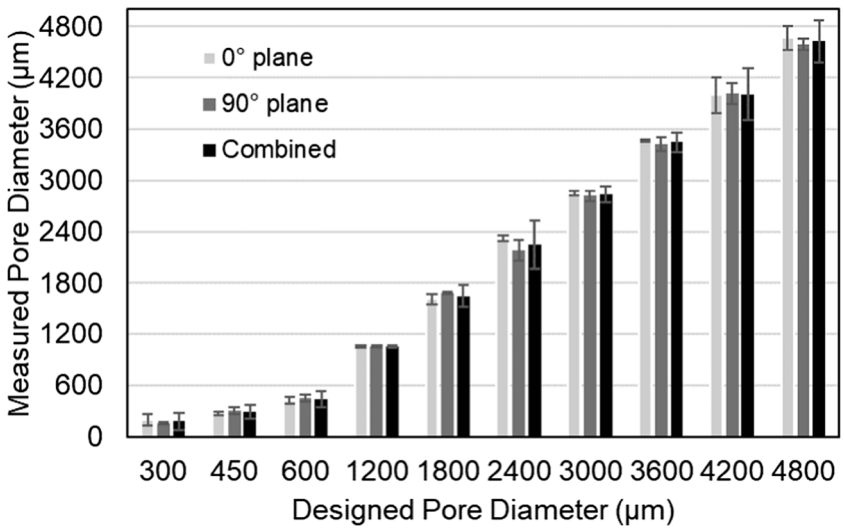

Fig. 5 Comparison of the pore diameter measurement and uncertainty using different viewing directions in 2D radiography and the effect of using both planes for a more accurate value of the pore diameter

uncertainty throughout the equation and into the uncertainty in the percent difference, δq, the general formula for error propagation was used:

$$\delta q = \sqrt{\left(\frac{\partial \mathrm{q}}{\partial \mathrm{x}}\delta x\right)^2 + \left(\frac{\partial \mathrm{q}}{\partial \mathrm{y}}\delta y\right)^2} \tag{7}$$

Mechanical Testing

Uniaxial tension tests were performed on six to nine samples with each of the pore geometries and dense samples using an electromechanical load frame (MTS Criterion Model 45) with a 150 kN load cell. Quasi-static tension tests were performed under displacement control using an applied strain rate on the order of 10^{-4} s^{-1}. The surface deformation fields were measured using 3D digital image correlation (DIC), a non-contact surface strain measurement technique (Vic3D software, Correlated Solutions). The gauge regions of the machined samples were painted with flat white basecoat with a random black speckle on top. Images of the sample during loading were taken at a rate of 1 Hz using two digital cameras (Point Grey GRAS-50S5M-C) and data capture software (VicSnap, Correlated Solutions). A calibration target with a 14 × 9 dot pattern and 3 mm spacing between dots was used to calibrate relative position of the cameras with respect to each other. A subset size of 29 pixels and a step size of 7 pixels was used for the surface deformation analysis of the images. To compute the evolution of vertical strain in the gauge region during post-processing, a vertical virtual extensometer of length 24 mm was used. The engineering stress was calculated as a function of applied force and the cross-sectional area of each sample using the measured outer diameter of the gauge region (i.e., not considering a reduced cross-sectional area due to the introduction of a pore).

Results and Discussion

Bulk Porosity Analysis

Using the Archimedes density technique, the average bulk porosity of the dense samples was found to be 0.60 ± 0.2%. The bulk measure of porosity remained relatively constant up to the maximum designed 4800 μm pore samples, which had an average bulk porosity of 0.88 ± 0.2%. The 4200 μm pore samples had the largest measured bulk porosity of 0.95 ± 0.1%. Archimedes can only provide information on bulk porosity and does not provide any information on the size of pores, distribution of pores, or morphology of pores. Additionally, the Archimedes method does not account for the true volume of the intentional internal pore space as these pores also include trapped powder that remains after the fabrication, which does not aid mechanical properties but adds uncertainty in this measurement technique. However, the low bulk porosity measured in the dense samples provides confidence that any changes in the mechanical properties of the samples with the intentional pores included in this study can be attributed to the intentional pore present at the center of each sample (i.e., not random porosity throughout, as this was not found in any of the measurement methods).

Characterization of Intentional Pores

The X-ray CT measurements gave the most accurate measurement of the morphology of the pores when comparing the three local analysis techniques used because of the ability to resolve 3D features, as shown in Fig. 6. The CT analysis also allowed for the measurement of the diameter of the pores in the XY plane, shown in Fig. 7, as opposed to the vertical build direction planes evaluated in the 2D analysis. It should be noted that in all the measurement techniques the 150 μm designed pore was not resolvable, likely due to melt pool spreading during fabrication, closing the pore, and is excluded from the analysis. Taking the X-ray CT reconstructed data as the measurement of the actual pore diameter, and comparing this to the designed pore geometry in the CAD drawings, the average percent error of all resolvable pore diameters was −4.9%, and − 2.4% when the smallest resolvable pore (300 μm) is excluded. This indicates that smaller pores were more challenging to make per the design than larger

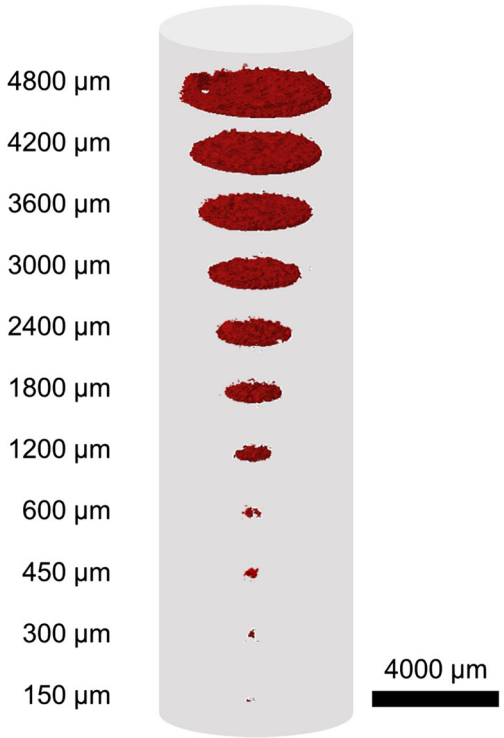

Fig. 6 3D X-ray CT reconstruction of the eleven pores in the witness sample within the 6 mm diameter cylinder

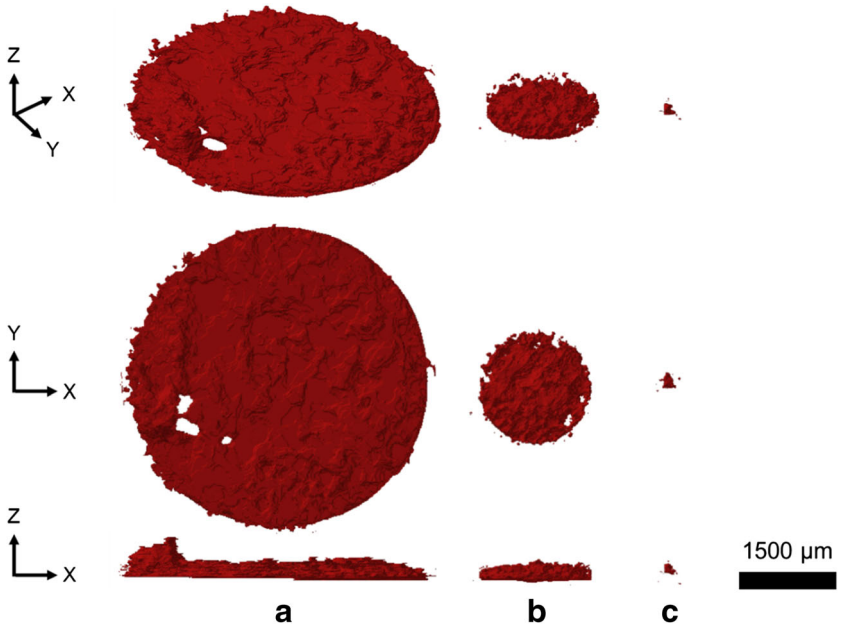

Fig. 7 X-ray CT images of the reconstructed pores in different planes for the (**a**) 4800 μm, (**b**) 1800 μm, and (**c**) 300 μm pores

pores, which is likely due to the flow of the meltpool in the build plane and dross formation in the vertical build direction. However, these measurements indicate that in this study, pores whose designed diameters were larger than 300 μm can be assumed to have been accurately fabricated within the tensile sample, and any size effects on mechanical properties can be interpreted in terms of the designed pore diameter. This is opposed to the 2D cross-section and radiograph methods, which gave average percent errors of −11.6% and − 13.1% compared to the designed pore diameter, respectively, but have other measurement artifacts that could impact their results discussed below. Therefore, in all discussion and analysis below, the designed pore diameter is referred to, since X-ray CT found good agreement between the designed and actual pore diameters.

Taking the diameter measurements from 3D X-ray CT as the baseline with which to compare the two 2D analysis methods, it was found that for pores designed with a diameter of 450 to 1200 μm, the OM cross-section analysis more accurately resolved the pore diameters than 2D radiography. However, for pores 1800 μm or larger, the 2D radiography method provided more accurate measurement of the pores compared to the 2D cross-section method. These trends are shown in Fig. 8, where the cross-section with OM method tended to overestimate the pore diameter for the smaller pores, while the 2D radiography method always underestimated the pore diameter, especially the 300 and 450 μm pores. The consistent underestimate of diameter in the 2D radiography method is a result of two main factors: the difficulty in differentiating the un-melted trapped powder at the edges of the pores, which have the same density, and therefore grayscale values, as the solid material, resulting in challenges in defining the full geometrical extents of the pore; and the fact that the 2D images are a projection of 3D samples where the pores are surrounded by dense material resulting in gradient of grayscale values along the 2D cross-sectional projection that can also be difficult to threshold, as shown in Fig. 3. For pores larger than 1800 μm, where the pore edges are close to the 6 mm outer diameter of the witness sample, the radiograph analysis was very close to the X-ray CT method. Using

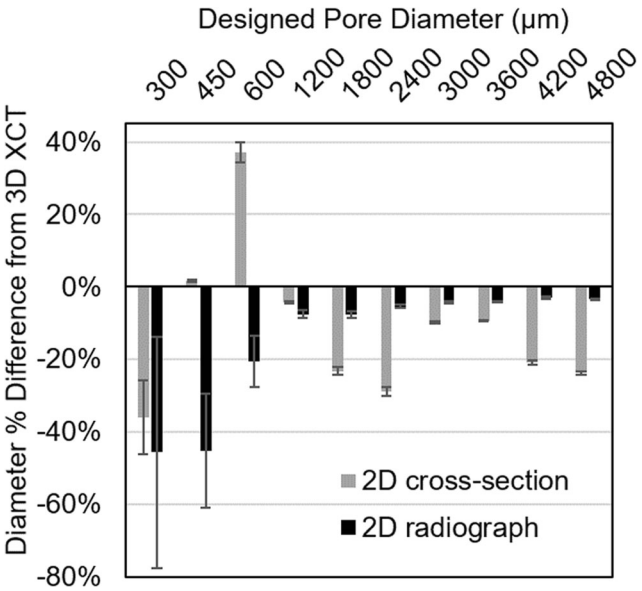

Fig. 8 Comparison of the 2D analysis techniques as related to their similarity with the pore diameter measured in the 3D X-ray CT analysis using percent difference. A positive percentage indicates the 2D measurement was larger than the 3D X-ray CT measurement and a negative percentage indicates the 2D measurement was smaller than 3D X-ray CT measurement. Both methods are shown to more likely result in a smaller pore diameter measurement then that by 3D X-ray CT

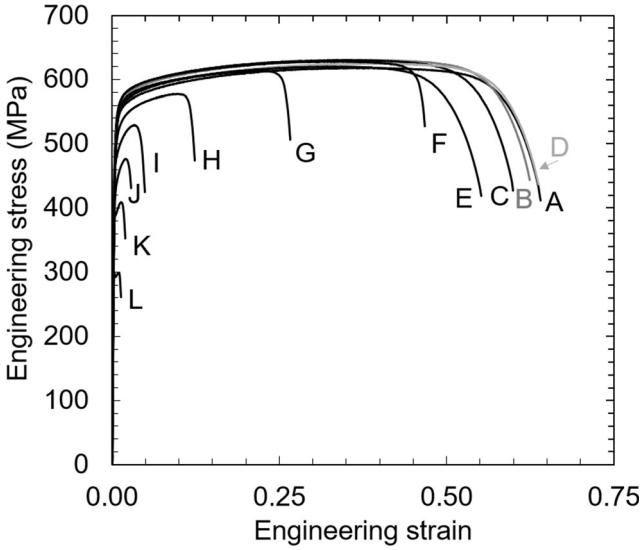

Fig. 9 Representative engineering stress-strain curves for samples with each initial pore diameter. A is representative of the dense samples, while B-L correspond to samples with increasing pore diameters. See Table 3 for nomenclature of B-L pore diameters

percent difference to compare measurements of the pores larger than 1800 μm, the 2D radiograph measured average diameter was only 4% smaller than the X-ray CT-measured diameters, and the diameter measured using the OM method was 19% smaller than the X-ray CT diameter. Given that smaller pores are more prevalent in AM builds, the cross-section with the OM analysis technique provided more relevant information in the analysis of the intentionally embedded pore diameters, although there is no consistent trend of over or under estimating the pore size. However, capturing the pore geometry with OM can be a challenge and can result in skewed data for two primary reasons: first, if the pore is not sliced and viewed exactly in the center plane, this will result in an underestimate of diameter; second, if the sample is not sectioned and polished exactly parallel to the build axis, the pore will be viewed at an angle, resulting in a possible overestimate of the pore dimensions at the location viewed.

Tensile Testing

Uniaxial tension testing of the dense samples and those with internal pores revealed clear trends with respect to mechanical properties as a function of pore diameter in the 6 mm diameter sample, as shown in Fig. 9. The change in mechanical behavior was a function of the pore size within the constant outer diameter of the gauge region. The increasing pore size also

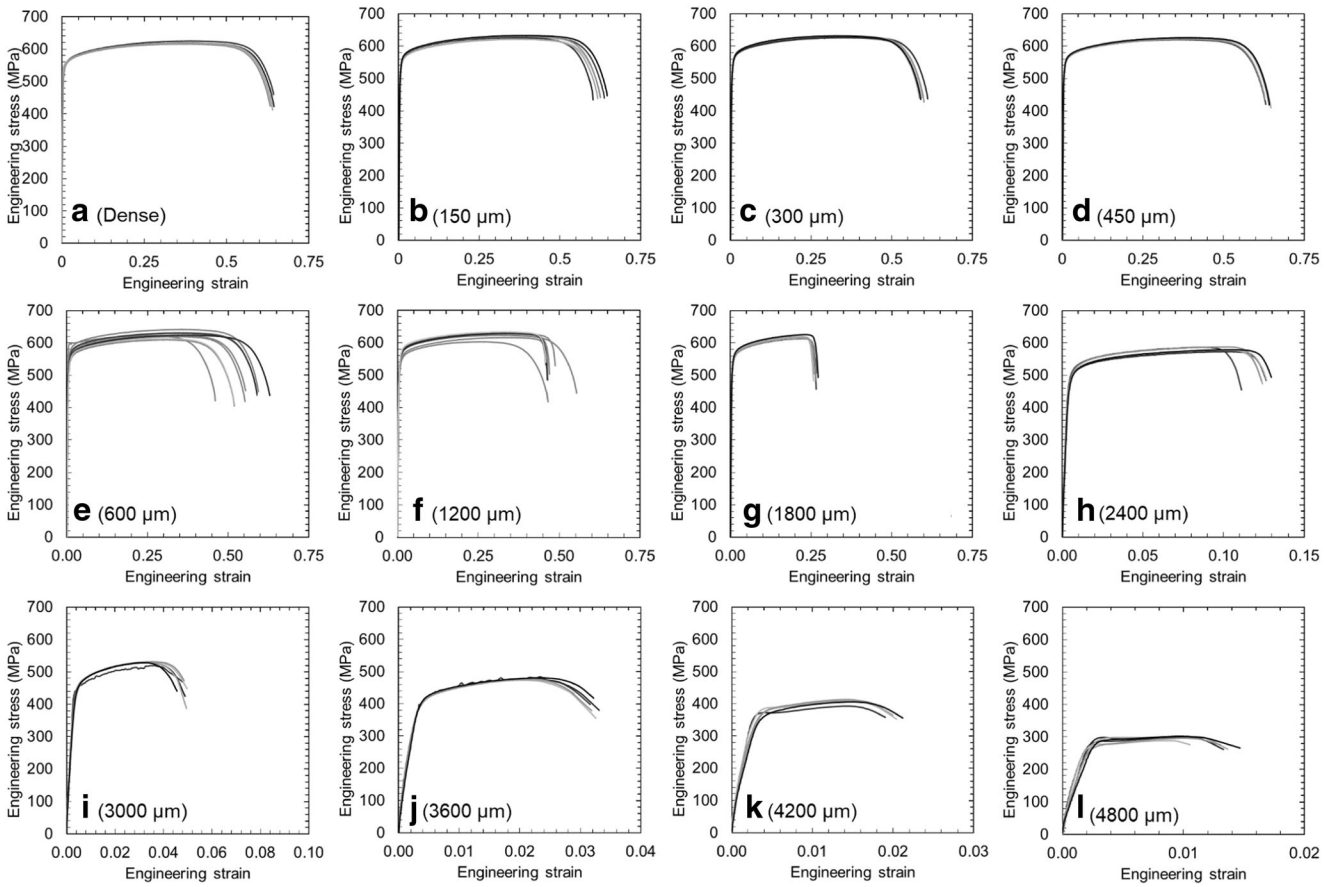

Fig. 10 Engineering stress-strain plots for each uniaxial tension test. Note that the x-axis scales are the same in **a**-**g**, but adjusted in **h**-**l**, while the y-axis sclaes are the same in **a**-**l**

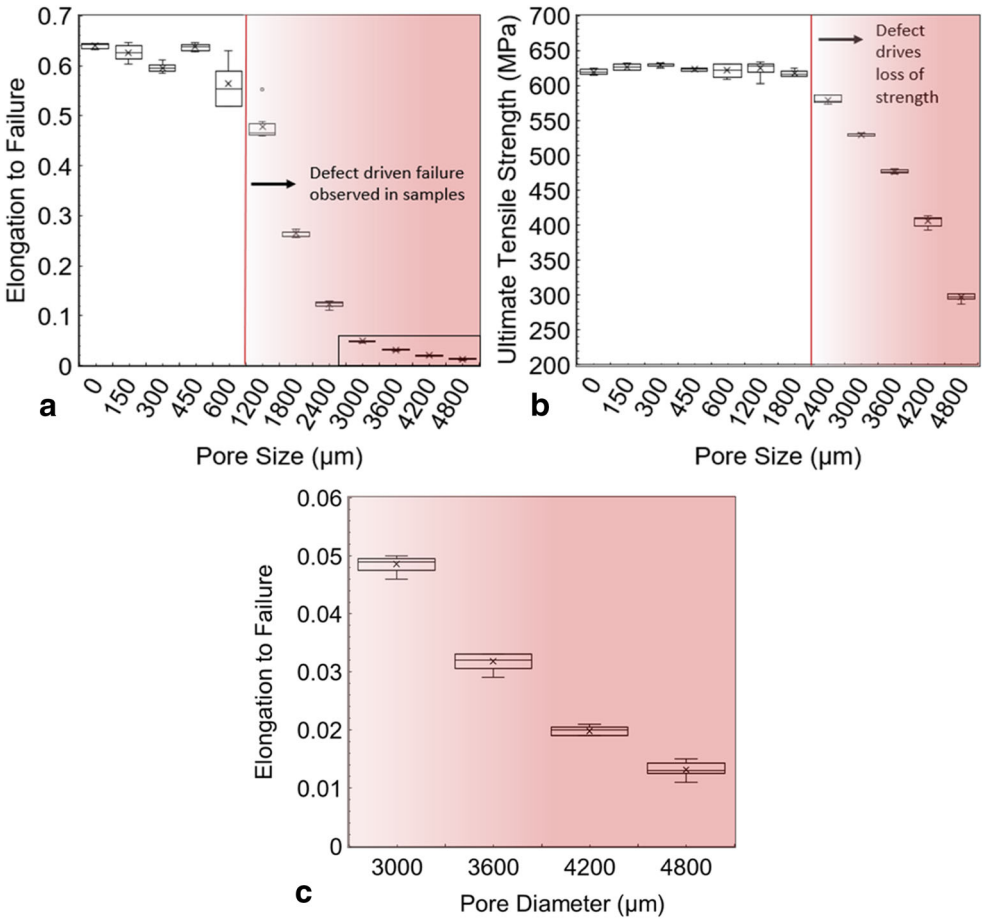

Fig. 11 Box plots displaying the minimum, maximum, first and third quartiles, exclusive median (central line), and mean (x) of (**a**) tensile elongation to failure and (**b**) ultimate tensile strength as a function of pore diameter with the pore diameter at which each of these properties begins to be negatively impacted shown. Inset of (**a**) is given in (**c**)

corresponds to a decreasing number of grains in the remaining cross-sectional area. The average grain area in the XY plane of the 316L material in this study was measured to be 584 μm^2 or 19.3 μm in diameter. In the fully dense samples, this results in more than 48,000 grains within the cross-sectional area of the 6 mm gauge region of the tensile samples, which reduces to around 2000 grains in samples with a 4800 μm pore, the largest intentional pore evaluated in the study. Thus, this work studies the impact of pore size with respect to the component size (e.g., thick and thin components), while still evaluating a bulk number of grains within a cross-section.

The presence of the pre-existing pore did not affect the material strength or ductility of the samples until the pore was greater than or equal to 600 μm in diameter, as shown in Fig. 10. At a pore diameter of 600 μm, corresponding to 10% of the cross-sectional diameter, the inclusion of the pore resulted in significant spread in the data compared to samples with smaller pores or no pores. At a pore diameter of 1200 μm, 20% of the cross-sectional diameter, seven of the nine samples failed at the pore. It was evident when a sample did fail at a pore because the pore, surrounded by shear lips, was clearly visible on the fracture surfaces in these samples. Once the initial pore was 1800 μm in diameter, 30% of the cross-sectional diameter, there was a repeatable reduction in the elongation to failure of the samples to 26.5 ± 0.5% compared to 64 ± 0.5% in the dense samples. Increasing pore diameters resulted in decreased elongation to failure for all pore diameters exceeding 1800 μm, as shown in Fig. 11a. The samples with the largest pore, 4800 μm in diameter, had tensile elongations to failure of under 1.5%.

Deterioration of material strength occurred for pores greater than or equal to 2400 μm in diameter within the 6 mm diameter gauge region. The UTS of the material dropped from 619 ± 3 MPa in the dense samples to 580 ± 5 MPa for samples with an internal pore 2400 μm in diameter. The strength of the material continued to decrease with increasing pore diameter above 2400 μm all the way to a UTS of 297 ± 5 MPa in the sample with the maximum pore diameter of 4800 μm as shown in Fig. 11b.

These findings indicate that L-PBF 316L is defect insensitive up to large pore sizes, with respect to sample dimensions. Samples with a gauge diameter of 6 mm and an internal pore diameter up to 2400 μm maintain the experimentally determined UTS of wrought 316L [38], while samples with a pore diameter of up to 3600 μm maintain the experimentally determined UTS of as-cast 316L [39]. Additionally, the uniform elongation of the 6 mm gauge diameter sample exceeds that required of wrought material even with a 1200 μm intentional pore.

Conclusion

The current work evaluated the effect of internal pores on the tensile properties of L-PBF 316L and compared common techniques used to evaluate internal pores in metallic components. This study, which is unique in both the material evaluated and the fact that pores of varying sizes were directly fabricated inside of samples to link pore geometry to mechanical properties, provides the following primary conclusions:

- The tensile strength of L-PBF 316L was shown to be insensitive of significant defects. Penny-shaped intentionally introduced pores with a height on the order of 180 μm within tensile samples with a gauge diameter of 6 mm only began to impact ultimate tensile strength when the pore diameter was 2400 μm, or 16% of the cross-sectional sample area.
- The tensile elongation to failure was slightly more sensitive to the internal defects as the elongation decreased substantially when the pore diameter was 1800 μm in diameter or 9% of the cross-sectional sample area.
- Samples with a pore diameter of 450 μm and smaller behaved very similarly to dense samples, with the mechanical properties showing very good repeatability, no drop-off in strength, and only 9% reduction in elongation to failure. The 600 μm and 1200 μm pore diameters led to significant scatter in the elongation to failure behavior.
- Internal pores were most accurately characterized using the 3D X-ray CT technique, which could capture pore morphology, pore size, pore location, and if multiple pores were present, the spatial distributions of pores and pore sizes; however, if this method is not an option, 2D cross-section analysis with OM of pores 1200 μm and smaller provides data that captures the geometry of the pores within 20% on average. For larger pores or internal features, 2D radiographs provide fast and accurate geometry information.

Acknowledgements The financial support provided by the National Science Foundation through award number CMMI-1652575 is gratefully acknowledged. Any opinions, findings, and conclusions or recommendations expressed in this material are those of the authors and do not necessarily reflect the views of the National Science Foundation. The samples were fabricated at Penn State's Center for Innovative Materials Processing through Direct Digital Deposition (CIMP-3D). The authors also express their gratitude to the staff of the Center for Quantitative Imaging (CQI) at Penn State for their help with X-ray CT work.

References

1. DebRoy T, Wei HL, Zuback JS, Mukherjee T, Elmer JW, Milewski JO, Beese AM, Wilson-Heid A, De A, Zhang W (2018) Additive manufacturing of metallic components – process, structure and properties. Prog Mater Sci 92. https://doi.org/10.1016/j.pmatsci.2017.10.001
2. Sun S, Brandt M, Easton M (2017) Powder bed fusion processes: An overview. In: Laser Additive Manufacturing. pp 55–77
3. Gu DD, Meiners W, Wissenbach K, Poprawe R (2012) Laser additive manufacturing of metallic components: materials, processes and mechanisms. Int Mater Rev 57:133–164. https://doi.org/10.1179/1743280411Y.0000000014
4. Cunningham R, Nicolas A, Madsen J, Fodran E, Anagnostou E, Sangid MD, Rollett AD (2017) Analyzing the effects of powder and post-processing on porosity and properties of electron beam melted Ti-6Al-4V. Mater Res Lett 5:516–525. https://doi.org/10.1080/21663831.2017.1340911
5. Li R, Liu J, Shi Y, Du M, Xie Z (2010) 316L stainless steel with gradient porosity fabricated by selective laser melting. J Mater Eng Perform 19:666–671. https://doi.org/10.1007/s11665-009-9535-2
6. Sames WJ, List FA, Pannala S, Dehoff RR, Babu SS (2016) The metallurgy and processing science of metal additive manufacturing. Int Mater Rev 61:315–360. https://doi.org/10.1080/09506608.2015.1116649
7. King WE, Barth HD, Castillo VM, Gallegos GF, Gibbs JW, Hahn DE, Kamath C, Rubenchik AM (2014) Observation of keyhole-mode laser melting in laser powder-bed fusion additive manufacturing. J Mater Process Technol 214:2915–2925. https://doi.org/10.1016/j.jmatprotec.2014.06.005
8. Vilaro T, Colin C, Bartout JD (2011) As-fabricated and heat-treated microstructures of the Ti-6Al-4V alloy processed by selective laser melting. Metall Mater Trans A 42:3190–3199. https://doi.org/10.1007/s11661-011-0731-y
9. Cunningham R, Narra SP, Montgomery C, Beuth J, Rollett AD (2017) Synchrotron-based X-ray microtomography characterization of the effect of processing variables on porosity formation in laser power-bed additive manufacturing of Ti-6Al-4V. Jom 69:479–484. https://doi.org/10.1007/s11837-016-2234-1
10. Morrow BM, Lienert TJ, Knapp CM, Sutton JO, Brand MJ, Pacheco RM, Livescu V, Carpenter JS, Iii GTG (2018) Impact of defects in powder feedstock materials on microstructure of 304L and 316L stainless steel produced by additive manufacturing. Metall Mater Trans A. https://doi.org/10.1007/s11661-018-4661-9
11. Whittenberger EJ, Rhines FN (1952) Origin of porosity in castings of magnesium-aluminum and other alloys. J Met 4:409–420
12. Gong H, Rafi K, Gu H, Janaki Ram GD, Starr T, Stucker B (2015) Influence of defects on mechanical properties of Ti-6Al-4V components produced by selective laser melting and electron beam melting. Mater Des 86:545–554. https://doi.org/10.1016/j.matdes.2015.07.147
13. Mertens A, Reginster S, Paydas H, Contrepois Q, Dormal T, Lemaire O, Lecomte-Beckers J (2014) Mechanical properties of alloy Ti–6Al–4V and of stainless steel 316L processed by selective laser melting: influence of out-of-equilibrium microstructures. Powder Metall 57:184–189. https://doi.org/10.1179/1743290114Y.0000000092
14. Carlton HD, Haboub A, Gallegos GF, Parkinson DY, MacDowell AA (2016) Damage evolution and failure mechanisms in additively manufactured stainless steel. Mater Sci Eng A 651:406–414. https://doi.org/10.1016/j.msea.2015.10.073
15. Edwards P, Ramulu M (2014) Fatigue performance evaluation of selective laser melted Ti–6Al–4V. Mater Sci Eng A 598:327–337. https://doi.org/10.1016/j.msea.2014.01.041
16. Stef J, Poulon-Quintin A, Redjaimia A, Ghanbaja J, Ferry O, De Sousa M, Gouné M (2018) Mechanism of porosity formation and influence on mechanical properties in selective laser melting of Ti-6Al-4V parts. Mater Des doi: https://doi.org/10.1016/j.matdes.2018.06.049

17. Spierings AB, Schneider M, Eggenberger R (2011) Comparison of density measurement techniques for additive manufactured metallic parts. Rapid Prototyp J 17:380–386. https://doi.org/10.1108/13552541111156504
18. Haynes R (1971) Effect of porosity content on the tensile strength of porous materials. Powder Metall 14:64–70. https://doi.org/10.1179/pom.1971.14.27.004
19. Haynes R (1977) A study of the effect of porosity content on the ductility of sintered metals. Powder Metall 20:17–20. https://doi.org/10.1179/pom.1977.20.1.17
20. Gurson AL (1977) Continuum theory of ductile rupture by void nucleation and growth: part I—yield criteria and flow rules for porous ductile media. J Eng Mater Technol 99:2. https://doi.org/10.1115/1.3443401
21. McClintock FA (1968) A criterion for ductile fracture by the growth of holes. J Appl Mech 35:363–371. https://doi.org/10.1115/1.3601204
22. Fadida R, Shirizly A, Rittel D (2018) Dynamic tensile response of additively manufactured Ti6Al4V with embedded spherical pores. J Appl Mech 85:1–10. https://doi.org/10.1115/1.4039048
23. Slotwinski JA, Garboczi EJ, Hebenstreit KM (2014) Porosity measurements and analysis for metal additive manufacturing process control. J Res Natl Inst Stand Technol 119:494–528. https://doi.org/10.6028/jres.119.019
24. Yusuf S, Chen Y, Boardman R, Yang S, Gao N (2017) Investigation on porosity and microhardness of 316L stainless steel fabricated by selective laser melting. Metals (Basel) 7:64. https://doi.org/10.3390/met7020064
25. Thompson A, Maskery I, Leach RK (2016) X-ray computed tomography for additive manufacturing: a review. Meas Sci Technol 27. https://doi.org/10.1088/0957-0233/27/7/072001
26. De Chiffre L, Carmignato S, Kruth JP, Schmitt R, Weckenmann A (2014) Industrial applications of computed tomography. CIRP Ann - Manuf Technol 63:655–677. https://doi.org/10.1016/j.cirp.2014.05.011
27. 3D Systems ProX® DMP 320. https://www.3dsystems.com/3d-printers/production/prox-dmp-320. Accessed 21 Feb 2017
28. ASTM International (2018) E1019–18: Standard Test Methods for Determination of Carbon, Sulfur, Nitrogen, and Oxygen in Steel and in Steel, Iron, Nickel, and Cobalt Alloys by Various Combustion and Fusion Techniques
29. ASTM International (2017) E1097–12: Standard Guide for Determination of Various Elements by Direct Current Plasma Atomic Emission Spectrometry
30. Riemer A, Leuders S, Thöne M, Richard HA, Tröster T, Niendorf T (2014) On the fatigue crack growth behavior in 316L stainless steel manufactured by selective laser melting. Eng Fract Mech 120:15–25. https://doi.org/10.1016/j.engfracmech.2014.03.008
31. ASTM International (2016) E8/E8M - 16a: Standard Test Methods for Tension Testing of Metallic Materials
32. Frazier WE (2014) Metal additive manufacturing: a review. J Mater Eng Perform 23:1917–1928. https://doi.org/10.1007/s11665-014-0958-z
33. ASM International (2003) Alloy Digest
34. Schneider CA, Rasband WS, Eliceiri KW (2012) NIH image to ImageJ: 25 years of image analysis. Nat Methods 9:671–675. https://doi.org/10.1038/nmeth.2089
35. du Plessis A, Yadroitsev I, Yadroitsava I, Le Roux SG (2018) X-ray microcomputed tomography in additive manufacturing: a review of the current technology and applications. 3D Print Addit Manuf 5:1–21. https://doi.org/10.1089/3dp.2018.0060
36. Feldkamp LA, Davis LC, Kress JW (1984) Practical cone-beam algorithm. J Opt Soc Am A 1:612–619. https://doi.org/10.1364/JOSAA.1.000612
37. Thermo Fisher Scientific (2018) Avizo Software 9 User's Guide. 61–101
38. Mower TM, Long MJ (2016) Mechanical behavior of additive manufactured, powder-bed laser-fused materials. Mater Sci Eng A 651:198–213. https://doi.org/10.1016/j.msea.2015.10.068
39. Wang YM, Voisin T, McKeown JT, Ye J, Calta NP, Li Z, Zeng Z, Zhang Y, Chen W, Roehling TT, Ott RT, Santala MK, Depond PJ, Matthews MJ, Hamza AV, Zhu T (2017) Additively manufactured hierarchical stainless steels with high strength and ductility. Nat Mater. https://doi.org/10.1038/nmat5021